Phase-shift estimation in sinusoidally illuminated images for lateral superresolution

Sapna A. Shroff,[1,2,3,*] **James R. Fienup,**[1,2,3] **and David R. Williams**[2,3]

[1]*Electrical and Computer Engineering, University of Rochester, Rochester, New York 14627, USA*
[2]*Institute of Optics, University of Rochester, Rochester, New York 14627, USA*
[3]*Center for Visual Science, University of Rochester, Rochester, New York 14627, USA*
**Corresponding author: sapna@optics.rochester.edu*

Received May 21, 2008; accepted November 17, 2008;
posted December 17, 2008 (Doc. ID 96472); published January 30, 2009

Sinusoidally patterned illumination has been used to obtain lateral superresolution and axial sectioning in images. In both of these techniques multiple images are taken with the object illuminated by a sinusoidal pattern, the phase of the sinusoidal illumination being shifted differently in each image. The knowledge of these phase shifts is critical for image reconstruction. We discuss a method to estimate this phase shift with no prior knowledge of the shifts. In postprocessing we estimate randomly introduced, unknown phase shifts and process the images to obtain a superresolved image. Results of computer simulations are shown. © 2009 Optical Society of America

OCIS codes: 100.3020, 100.6640, 050.5080, 170.0180, 070.0070, 110.4850.

1. INTRODUCTION

The lateral resolution of any imaging system is limited by the wavelength of imaging and the numerical aperture of the system. But this limit holds only for uniform illumination and objects with linear absorption and emission characteristics. It is possible to break this limit by imaging outside these constraints. Many techniques have been developed to obtain superresolution in images by using off-axis illumination, nonlinear absorption and emission of light, and nonuniform illumination of the object [1–16].

Structured illumination [1–5] is one such method where the object is illuminated with a sinusoidal pattern instead of the conventional uniform illumination. The Fourier transform of the intensity of a sinusoid is three impulses—one at the origin and the other two at the positive and negative spatial frequency of the sinusoid. Therefore, when a sinusoidal illumination is incident on an object, the Fourier transform of the image consists of three replicas of the object Fourier transform, each centered at one of the three impulses. So in addition to the conventional object Fourier transform centered at the origin in Fourier space, now there are two additional copies shifted to the spatial frequency of the sinusoidal illumination. These shifted copies, within the passband of the imaging system, carry portions of the object Fourier transform that would conventionally lie outside the passband and thus give superresolution information beyond the diffraction limit.

To separate these three overlapping replicas of the object Fourier transform, three or more images of the same object are taken with the phase of the sinusoid shifted by distinct values in each image. After separating the shifted replicas of the object Fourier transform, we move them back to their true positions in spatial frequency space and combine them with the unshifted version, with appropriate weighting, to obtain an extended Fourier transform and an image superresolved beyond the diffraction limit. These reconstructions have superresolution along the direction perpendicular to the fringes of the sinusoid: e.g., a vertical fringe pattern increases the resolution along the horizontal axis. The same procedure can be repeated with the orientation of the sinusoidal illumination rotated by, say, 60° and 120° to obtain superresolution in all directions in Fourier space. The amount of superresolution obtained is directly proportional to the spatial frequency of the sinusoidal illumination. Therefore, assuming linear absorption and emission, up to twice the diffraction-limited resolution can be obtained using this method.

As far as we know, sinusoidal illumination imaging for superresolution and axial sectioning has only been implemented on stationary specimens such as fixed slides on a vibration-free microscope [1–5,17–19]. The processing requires very accurate knowledge of the phase shifts of the sinusoid in each image in order to recover the three overlapping copies of the object Fourier transform. Usually these phase shifts are imparted in definite known steps using expensive, calibrated, precision actuation equipment.

We are interested in imaging moving objects, such as the *in vivo* retina, which show substantial interframe rigid body motion. Hence it is not possible to impart known phase shifts of definite step sizes to such a randomly moving object specimen. In this paper we discuss a postprocessing method of estimating completely unknown, randomly introduced phase shifts and conditions wherein this method can give reliable results. Our technique applies for any orientation or spatial frequency of the sinusoidal illumination. We can also estimate the orientation and spatial frequency of the sinusoidal illumination if they are unknown. We also provide simulation results. Our experimental results on a microscope follow in a paper to be published. We do not explicitly discuss the optical sectioning application of sinusoidally illuminated images [17–19] in this paper, but the very same phase-shift estimates are also critical for sectioning, and our estimation method remains valid for sectioning with no need for modifications.

2. SUPERRESOLUTION WITH SINUSOIDAL ILLUMINATION

Here we assume interaction for light absorption and emission linear in intensity. We demonstrate the case of incoherent illumination such as a metal halide lamp and incoherent fluorescent emission. The sinusoidal pattern could be produced by a grating in the illumination path imaged onto the object.

The phase estimation analysis that follows is also applicable to the case where a coherent laser illumination is used to project sinusoidal fringes on a fluorescent object. Our method should also be valid for coherent illumination and coherent imaging, which is the case of nonfluorescent objects under coherent laser fringe illumination. This is not directly illustrated in this paper and will be dealt with in detail in a future paper.

A. Image Formation

The sinusoidal illumination pattern can be produced coherently by the interference of two tilted plane waves or incoherently by imaging a grating. For the case of coherent illumination (and a fluorescent object emitting incoherent light), assume a vertical fringe illumination field, $U_s(x,y)=\cos(2\pi f_o x+\phi_n)$, with a phase shift ϕ_n and spatial frequency $(f_o,0)$, where $f_o<f_c$, the coherent cutoff frequency of the system. The intensity of this sinusoidal illumination is

$$I_s(x,y)=\frac{1}{2}[1+\cos(4\pi f_o x+2\phi_n)], \tag{1}$$

which has spatial frequency $(2f_o,0)$ and phase shift $2\phi_n$. Depending on the method of illumination, the fringe contrast, m, may be less than unity and we have

$$I_s(x,y)=\frac{1}{2}[1+m\cos(4\pi f_o x+2\phi_n)]. \tag{2}$$

In most simulations shown in this paper we use $m=1$, assuming maximum contrast of the sinusoid.

For the case of incoherent imaging of a grating onto the fluorescent object, we assume that the illumination and imaging path optical transfer functions (OTFs) are given by $\mathcal{H}_1$ and $\mathcal{H}_2$, respectively. We assume that both optical paths pass through a single limiting lens giving a common coherent cutoff frequency limit, f_c. It should be noted that in the case of a double-pass system where the illumination and imaging takes place using the same lens, $\mathcal{H}_2(f_x,f_y)=\mathcal{H}_1(-f_x,-f_y)$. N such sinusoidally patterned images of the object are taken, where $N\geq 3$. The Fourier transform (approximated by a discrete Fourier transform in the computer) of the nth image, where $n=1,2,\ldots,N$, is given by [2,4]

$$\begin{aligned}\mathcal{G}_n(f_x,f_y)={}&\frac{1}{2}\mathcal{H}_1(0,0)\mathcal{H}_2(f_x,f_y)\mathcal{G}_g(f_x,f_y)\\&+\frac{m}{4}\mathcal{H}_1(2f_o,0)e^{i2\phi_n}\mathcal{H}_2(f_x,f_y)\mathcal{G}_g(f_x-2f_o,f_y)\\&+\frac{m}{4}\mathcal{H}_1(-2f_o,0)e^{-i2\phi_n}\mathcal{H}_2(f_x,f_y)\mathcal{G}_g(f_x+2f_o,f_y),\end{aligned} \tag{3}$$

where $\mathcal{G}_g$ is the object Fourier transform. This can be visualized as shown in Fig. 1.

The Fourier transform of each image can be seen to consist of three overlapping replicas of the object Fourier transform—one unshifted copy, proportional to $\mathcal{G}_g(f_x,f_y)$, and two shifted copies, proportional to $\mathcal{G}_g(f_x-2f_o,f_y)$ and $\mathcal{G}_g(f_x+2f_o,f_y)$. The two shifted versions carry the higher spatial frequencies that would conventionally lie outside the passband of the imaging system.

B. Reconstruction of Superresolved Image

It is essential to separate these three superimposed replicas of the object's Fourier transform in order to utilize the superresolution in the two shifted copies. The N images with different phase shifts in the sinusoidal illumination are used to perform this segregation. If one takes equally spaced phase shifts, then it is possible to arrive at a closed-form solution. However we cannot use this approach because we are interested in the case of randomly introduced phase shifts in the sinusoidal illumination. We separate the three superimposed terms on a pixel-by-pixel basis in the Fourier domain. For each pixel in the N image Fourier transforms, we consider a set of N linear equations given by

$$AX=B, \tag{4}$$

where

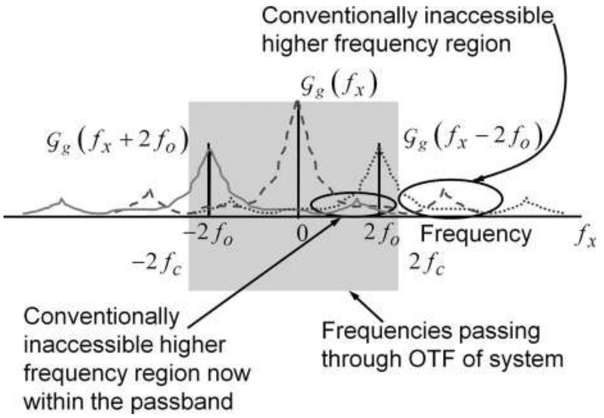

Fig. 1. Visualization of structured illumination image in Fourier domain.

$$A = \begin{bmatrix} \frac{1}{2}\mathcal{H}_1(0,0) & \frac{m}{4}\mathcal{H}_1(2f_o,0)e^{i2\phi_1} & \frac{m}{4}\mathcal{H}_1(-2f_o,0)e^{-i2\phi_1} \\ \frac{1}{2}\mathcal{H}_1(0,0) & \frac{m}{4}\mathcal{H}_1(2f_o,0)e^{i2\phi_2} & \frac{m}{4}\mathcal{H}_1(-2f_o,0)e^{-i2\phi_2} \\ \vdots & \vdots & \vdots \\ \frac{1}{2}\mathcal{H}_1(0,0) & \frac{m}{4}\mathcal{H}_1(2f_o,0)e^{i2\phi_N} & \frac{m}{4}\mathcal{H}_1(-2f_o,0)e^{-i2\phi_N} \end{bmatrix}_{N\times 3}, \tag{5}$$

$$X = \begin{bmatrix} \mathcal{H}_2(f_x,f_y)\mathcal{G}_g(f_x,f_y) \\ \mathcal{H}_2(f_x,f_y)\mathcal{G}_g(f_x-2f_o,f_y) \\ \mathcal{H}_2(f_x,f_y)\mathcal{G}_g(f_x+2f_o,f_y) \end{bmatrix}_{3\times 1}, \tag{6}$$

$$B = \begin{bmatrix} \mathcal{G}_1(f_x,f_y) \\ \mathcal{G}_2(f_x,f_y) \\ \vdots \\ \mathcal{G}_N(f_x,f_y) \end{bmatrix}_{N\times 1}. \tag{7}$$

The matrix of coefficients, A, must be known accurately in order to solve this equation. It includes the illumination OTF, $\mathcal{H}_1$, and modulation contrast, m, which are both common to all the images. It also contains the phase shifts, ϕ_n, which uniquely impart diversity to the N images. Hence the knowledge of ϕ_n is critical to the accuracy of the matrix A and the recovery of the three overlapping object Fourier transform replicas. If this phase shift is accurately known, then it is a simple matter of using singular value decomposition (SVD) and pseudoinverse [20] to invert A in order to recover the unknown overlapping terms in vector X.

The inverse Fourier transform of the unshifted term (first term in vector X), weighted by the imaging OTF, $\mathcal{H}_2(f_x,f_y)$, gives an image equivalent to the conventional image taken with uniform illumination. This is treated as one component image, I_{c1},

$$I_{c1}(f_x,f_y) = \mathcal{H}_2(f_x,f_y)\mathcal{G}_g(f_x,f_y), \tag{8}$$

containing low frequencies to be used later to form a composite superresolved image. The OTF for this component image is given by

$$otf_1(f_x,f_y) = \mathcal{H}_2(f_x,f_y). \tag{9}$$

The two shifted copies of the object Fourier transform (second and third terms in vector X), also weighted by the imaging OTF, $\mathcal{H}_2(f_x,f_y)$, are moved to their true positions in the spatial frequency domain as I_1' and I_1''. The subpixel shift is accomplished by Fourier methods,

$$\begin{aligned} I_1'(f_x,f_y) &= FT\{IFT[\mathcal{H}_2(f_x,f_y)\mathcal{G}_g(f_x-2f_o,f_y)] \\ &\quad \times \exp[-i2\pi(2f_o)x]\} \\ &= \mathcal{H}_2(f_x+2f_o,f_y)\mathcal{G}_g(f_x,f_y), \end{aligned} \tag{10}$$

$$\begin{aligned} I_1''(f_x,f_y) &= FT\{IFT[\mathcal{H}_2(f_x,f_y)\mathcal{G}_g(f_x+2f_o,f_y)] \\ &\quad \times \exp[+i2\pi(2f_o)x]\} \\ &= \mathcal{H}_2(f_x-2f_o,f_y)\mathcal{G}_g(f_x,f_y). \end{aligned} \tag{11}$$

We note here that in our simulation results we use a raised-cosine guard band padding the object to prevent errors in implementing the sub-pixel shift.

The two terms, I_1' and I_1'', are now added so as to form a two-component image Fourier transform, I_{c2}, which contains spatial frequencies above the diffraction limit in one direction in Fourier space,

$$I_{c2}(f_x,f_y) = [\mathcal{H}_2(f_x+2f_o,f_y) + \mathcal{H}_2(f_x-2f_o,f_y)]\mathcal{G}_g(f_x,f_y). \tag{12}$$

The OTF for I_{c2} is given by

$$otf_2(f_x,f_y) = [\mathcal{H}_2(f_x+2f_o,f_y) + \mathcal{H}_2(f_x-2f_o,f_y)]. \tag{13}$$

I_{c2} can be used, along with I_{c1}, to form a single superresolved image.

Similarly, this is repeated with the orientation of the sinusoidal illumination rotated by, say, 60° and 120°, to obtain additional component images, I_{c3} and I_{c5}, which provide low frequency information, having the OTF given by Eq. (9) and I_{c4} and I_{c6}, which provide high frequency superresolution along the 60° and 120° orientations in the Fourier domain, which have OTFs similar to Eq. (13), but rotated in Fourier space.

These six component images can be combined with appropriate weighting and OTF compensation to obtain the reconstructed image that has superresolution in all directions in the Fourier domain. We use the following filter [21] to OTF compensate and combine these six component images appropriately to obtain the reconstructed superresolved image:

$$I_{\mathrm{rec}}(x,y) = IFT\left\{ \sum_{i=1}^{M} \left[\frac{\hat{I}_{ci}(f_x,f_y) otf_i^{*}(f_x,f_y) \times \dfrac{\eta_i \Phi_O(f_x,f_y)}{\Phi_{Ni}}}{c + \displaystyle\sum_{j=1}^{M} |otf_j(f_x,f_y)|^2 \times \dfrac{\eta_j \Phi_O(f_x,f_y)}{\Phi_{Nj}}} \right] \right\}, \tag{14}$$

where M is the number of component images, I_{ci}, that go into forming the reconstruction. In the present case with three orientations we have $M=6$; each orientation of the sinusoidal illumination contributing two component images—one conventional and one with superresolution in one direction in Fourier space. The term Φ_O is the object power spectrum. This can be estimated from the conventional image using a generalized model for the object power spectrum [22–25]. We assume that the object is identical in all the component images; hence Φ_O is the same for all I_{ci} in this filter. Φ_{Ni} is the power spectrum of the noise in each component image; hence it is separately calculated for each I_{ci} [22–25]. For example it can be computed as the average power spectrum in the farthest corner of the Fourier transform of each I_{ci} outside the extent of otf_i. The constant η_i is a factor arising from the effect of estimation of I_{ci} by the SVD and pseudoinverse on the signal and noise. It depends on the number of images used to obtain each component image, I_{ci}, and on the phase shifts involved in the sinusoidal illumination in each image. For example, having multiple images with nearly identical phase shifts will result in less signal than equally spaced phase shifts. We have used $\eta_i=1$ in the simulations shown in this paper. The constant c may be used to weight the combination to give an image that might appear better to the observer in terms of trading off edge sharpness versus noise artifacts. In our simulations we set $c=1$, which is the minimum mean-squared error solution [21,26]. More details about the effect of signal-to-noise ratio (SNR) in this method of image reconstruction will be dealt with in another paper [27]. Next we will show how to estimate the phase shifts when they are unknown.

3. PHASE-SHIFT ESTIMATION FOR SINUSOIDALLY ILLUMINATED IMAGES

The phase shift of the sinusoidal illumination in each image can be estimated *a posteriori* in several ways [28,29]. One way is to average the image along the sinusoid fringe direction and then fit an ideal sinusoid to that average. The estimated phase is the phase of that sinusoid. But variations in the object intensity perturb this estimation. It is also difficult to average the image along the sinusoid if its orientation is not exactly parallel to one of the pixel directions on the CCD, since the interpolation of the values of pixels parallel to the orientation of the sinusoid introduces error in the phase-shift estimate. This technique also poses the difficulty that when the frequency of the sinusoidal illumination increases, the contrast of the fringe is reduced by a factor of $\mathcal{H}_1(2f_o,0)\mathcal{H}_2(2f_o,0)$ and the estimated phase becomes increasingly noisy.

Another technique is to vary the estimates of the phase shifts in such a way as to minimize the residual sinusoidal patterned artifacts in the reconstructed image [19]. This method is somewhat time-consuming and might need good initial estimates of the phase shift to avoid stagnation.

In our approach, we take the Fourier transform of the image of a sinusoidally illuminated object. In the Fourier domain we extract the phase of the shifted impulse arising from the spatial frequency of the sinusoidal illumination. The Fourier transform of the intensity of a vertical fringe has three peaks located at (0,0) $(2f_o,0)$, and $(-2f_o,0)$. The value of the Fourier transform, $\mathcal{G}_n$, given by Eq. (3), at $(2f_o,0)$ is

$$\begin{aligned}\mathcal{G}_n(2f_o,0) = {} & \frac{1}{2}\mathcal{H}_1(0,0)\mathcal{H}_2(2f_o,0)\mathcal{G}_g(2f_o,0) \\ & + e^{i2\phi_n}\frac{m}{4}\mathcal{H}_1(2f_o,0)\mathcal{H}_2(2f_o,0)\mathcal{G}_g(0,0) \\ & + e^{-i2\phi_n}\frac{m}{4}\mathcal{H}_1(-2f_o,0)\mathcal{H}_2(2f_o,0)\mathcal{G}_g(4f_o,0).\end{aligned} \tag{15}$$

In the above equation the third term, $e^{-i2\phi_n}(m/4)\times\mathcal{H}_1(-2f_o,0)\mathcal{H}_2(2f_o,0)\mathcal{G}_g(4f_o,0)$, is much smaller than the second term, $e^{i2\phi_n}(m/4)\mathcal{H}_1(2f_o,0)\mathcal{H}_2(2f_o,0)\mathcal{G}_g(0,0)$, because it is proportional to $|\mathcal{G}_g(4f_o,0)| \ll \mathcal{G}_g(0,0)$, for an extended object. Similarly the first term, $(1/2)\mathcal{H}_1(0,0)\mathcal{H}_2(2f_o,0)\mathcal{G}_g(2f_o,0)$, is much smaller than the second term, $e^{i2\phi_n}(m/4)\mathcal{H}_1(2f_o,0)\mathcal{H}_2(2f_o,0)\mathcal{G}_g(0,0)$, because $|\mathcal{G}_g(2f_o,0)| \ll \mathcal{G}_g(0,0)$ for an extended object as long as $m|\mathcal{H}_1(2f_o,0)|$ is not much smaller than $|\mathcal{H}_1(0,0)|$. Hence the first and third terms have a relatively small contribution to the Fourier transform of the image at the location $(2f_o,0)$ as long as f_o/f_c is not too close to 0 or 1, and the most significant contribution comes from the second term. Also $\mathcal{G}_g(0,0)$ and m are real valued, as are $\mathcal{H}_1(2f_o,0)$ and $\mathcal{H}_2(2f_o,0)$ when we use well-corrected optics with no aberrations. The dominant phase contribution to this equation then comes from $e^{i2\phi_n}$. Hence the phase shift of the sinusoidal illumination is approximately the phase of this peak, $\mathcal{G}_n(2f_o,0)$, in the Fourier transform of the image,

$$2\phi_n \sim \tan^{-1}\left\{\frac{\mathrm{imag}[\mathcal{G}_n(2f_o,0)]}{\mathrm{real}[\mathcal{G}_n(2f_o,0)]}\right\}. \tag{16}$$

Here the arctangent is computed using the atan2 function in MATLAB where the resulting phase lies between $-\pi$ and π. If the sinusoidal illumination intensity has a generalized spatial frequency $(2f_{ox},2f_{oy})$ for a rotated fringe pattern, then the phase shift can be similarly estimated from the phase of $\mathcal{G}_g(2f_{ox},2f_{oy})$.

If the spatial frequency of the sinusoidal illumination is very low, then the first and third terms in Eq. (15) may become nonnegligible as compared with the second term and their contribution then cannot be ignored, and the phase estimate might then be inaccurate. Also, at very high spatial frequencies of the sinusoidal illumination, approaching the cutoff frequency, the value of $\mathcal{H}_1(2f_o,0)\mathcal{H}_2(2f_o,0)$ will attenuate the sinusoid and lower its contrast substantially, and again the first term may not be negligible with respect to the second term, and the SNR will be low, decreasing the accuracy of the phase estimate. If the illumination and imaging OTFs have aberrations, then there might be some inaccuracy due to phase contributions from the aberrations. Also note that in the case of a double-pass system, where the illumination and imaging use the same lens, $\mathcal{H}_2(f_x,f_y) = \mathcal{H}_1(-f_x,-f_y)$, odd aberrations cancel out, and even aberrations double in value [30], affecting the phase-shift estimate.

4. SIMULATION RESULTS

To demonstrate this approach to sinusoidal phase-shift estimation, we simulated an incoherent sinusoidal illumination setup with three orientations of the sinusoid, rotated 0°, 120°, and 240°, and an incoherent image with no aberrations. We use a pristine object shown in Fig. 2(a) and its Fourier transform is shown in Fig. 2(b). It should be noted that all Fourier transforms displayed in this paper have been stretched to show details.

A. Accuracy of Phase-Shift Estimate

The accuracy of our phase-shift estimates varies with each orientation because when a significant component of the unshifted object Fourier transform overlaps with the peak of the shifted object Fourier transform, the contribution from the first term in Eq. (15) increases, decreasing the accuracy of the estimated phase. Our simulation object has numerous vertical and horizontal edges causing distinct horizontal and near-vertical streaks in the Fourier domain, as seen in Fig. 2(b), contributing to the variation in overlap with the orientation of the sinusoidal illumination of our object.

The accuracy of our estimates also varies with the spatial frequency of the sinusoidal illumination [28]. As shown in Fig. 3, we achieved accuracy better than 6×10^{-3} rad RMS for f_o/f_c between 15% and 85%. As expected, the error in the estimate increases at higher spatial frequencies of the sinusoidal illumination due to the reduction in the contrast of the sinusoidal illumination proportional to $m\mathcal{H}_1(2f_o,0)\mathcal{H}_2(2f_o,0)$. At lower f_o, error in the estimate increases because the value of the first term in Eq. (15) increases. Figure 4 shows the plot of RMS error in our estimates for different values of SNR when $f_o = 50\% f_c$. The accuracy in the estimates for the worst case was better than 1.5×10^{-3} rad RMS for moderate SNR. The error in our estimates increased up to 4×10^{-3} rad RMS for SNR in the range of 2–7. Figure 5 shows the same for a sinusoidal illumination frequency of $f_o = 91\% f_c$. Here the accuracy was better than 3×10^{-2} rad for moderate to high SNR. The error increased up to 0.95 rad for lower SNR in the range of 2–13 since for these levels of SNR the reduced contrast of the sinusoid is comparable to the noise floor. This range of error would definitely give rise to artifacts in the reconstructed image.

We demonstrate the effect of artifacts arising from error in phase-shift estimates in Fig. 6(a). The frequency of the sinusoidal illumination used here is at approximately 44% of cutoff frequency and there is no noise. We purposely introduced an error of 0.5 rad in the phase-shift estimate for one of three images (making the RMS error 0.2887 rad) with equally spaced phase shifts of 0, 2.0944, and 4.1888 rad, i.e., 0°, 120°, and 240° for one orientation

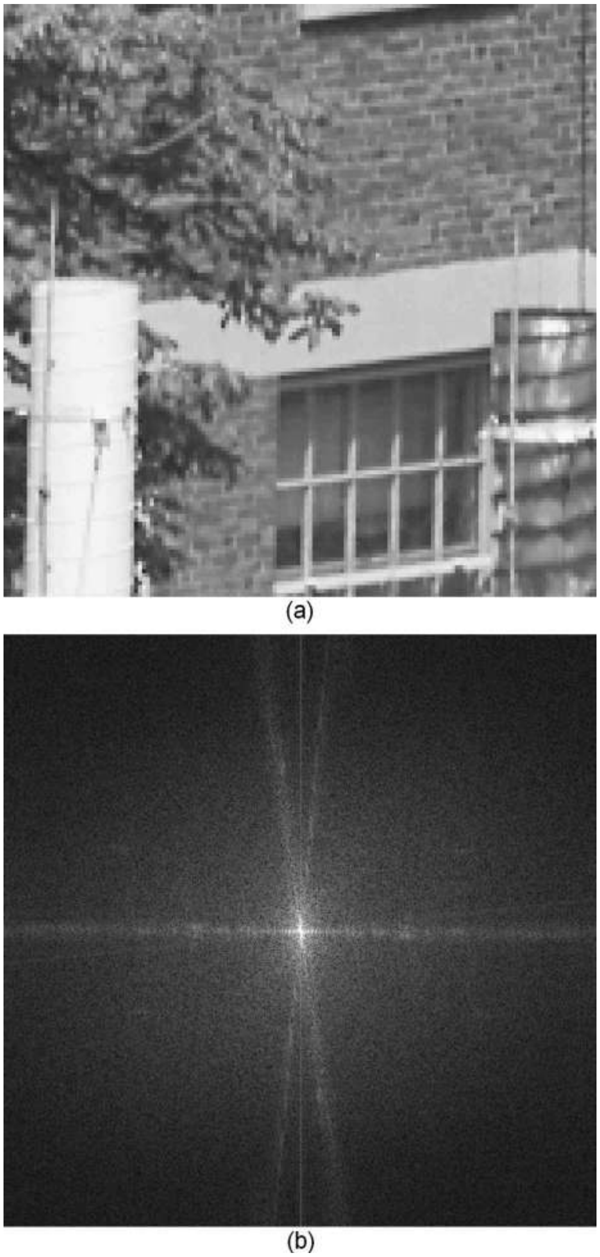

Fig. 2. (a) Pristine object; (b) Fourier transform of pristine object.

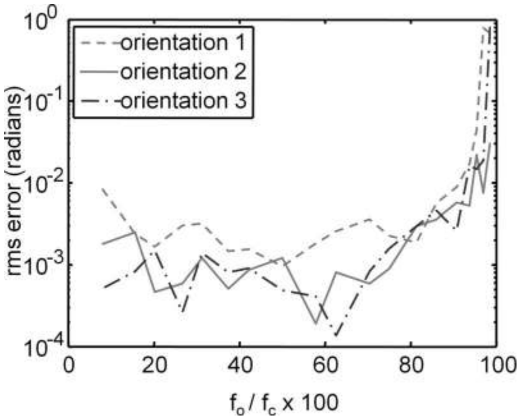

Fig. 3. RMS error in phase-shift estimate versus spatial frequency of sinusoidal illumination, f_o/f_c with no noise [28].

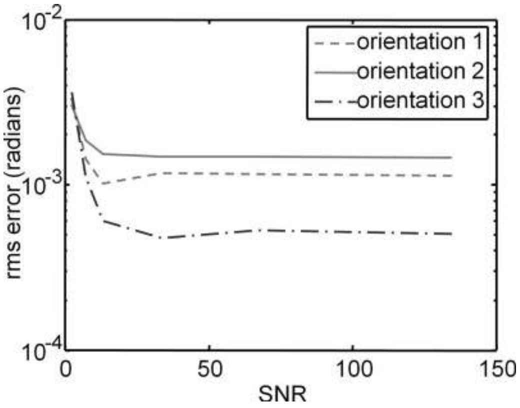

Fig. 4. RMS error in phase-shift estimate versus SNR for sinusoidal illumination with $f_o = 50\%\ f_c$ [28].

of the sinusoidal illumination used in this reconstruction. The residual fringes are parallel to that orientation of sinusoidal illumination. The estimated phase shifts are used to segregate the three overlapping terms contained in each sinusoidally illuminated image—the unshifted and two shifted copies of the object's Fourier transform. If the phase-shift estimate is inaccurate, this segregation remains incomplete. Therefore each incorrectly segregated term will now still contain some residual amount of overlapping shifted and unshifted copies of the object's Fourier transform. These will give rise to multiple residual peaks in each incorrectly segregated term. When these terms are combined, this gives rise to a reconstruction that contains multiple incorrect residual peaks in the Fourier domain. The Fourier transform of the reconstructed image in Fig. 6(b) shows distinct residual-peak artifacts, indicated by white arrows, which lie along the direction perpendicular to the orientation of the sinusoidal illumination which contained the error in the phase-shift estimate. These peaks in the Fourier domain translate into residual fringes in the image domain. The residual error of the phase shift, 0.2887 rad, which caused these artifacts, was purposely made large in order to produce distinctly noticeable artifacts. This phase-shift error is substantially larger than the errors of our phase-shift estimates plotted in Fig. 3–5, except for (a) very small f_o/f_c, (b) f_o/f_c close to unity, and (c) for SNR below 13 in Fig. 5 for which $f_o/f_c = 91\%$.

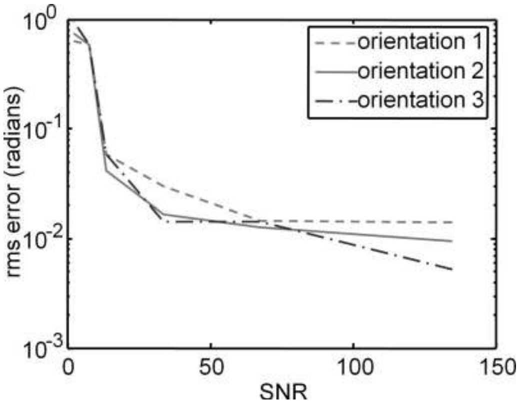

Fig. 5. RMS error in phase-shift estimate versus SNR for sinusoidal illumination with $f_o = 91\%\ f_c$ [28].

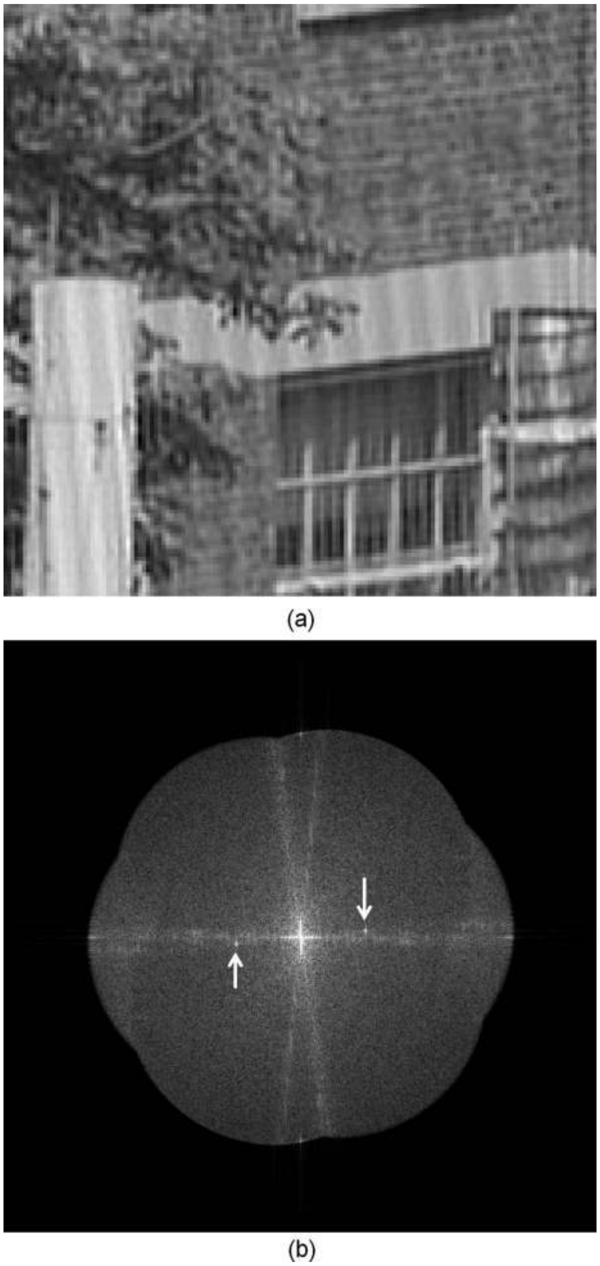

Fig. 6. (a) Reconstructed image with fringe artifacts due to a large error in the phase-shift estimate in one orientation of sinusoidal illumination; (b) Fourier transform of reconstructed image with residual peak artifacts (indicated by white arrows) due to a large error in the phase-shift estimate in one orientation of sinusoidal illumination.

The visibility of the artifact in the image is dependent on the contrast of the sinusoidal illumination and the error in the phase estimate. If the sinusoid has very low contrast, such as at very high frequencies of the sinusoidal illumination for the case of incoherently imaging a grating, then even if the residual peak artifacts are present in the Fourier domain, in the reconstructed image the resulting fringe artifacts may be very dim or may not even be visible. But for high contrast sinusoidal illumination at spatial frequencies such as 50% of cutoff, it is very important to have accurate estimates of the phase shift because residual peaks in the Fourier domain of the reconstruction will be strong enough to be visible as fringe artifacts in the image.

If the orientation or spatial frequency of the sinusoidal illumination is not known or is uncertain, then it is possible to approximately locate the peak, $\mathcal{G}_n(2f_o,0)$, in the Fourier domain of the structured illumination image by finding the local maximum (other than the dc peak at the origin), and upsample this peak to obtain its precise spatial frequency. We found from computer simulations that upsampling $\mathcal{G}_n(2f_o,0)$ to subpixel accuracy [31,32] significantly improves the accuracy of the phase-shift estimate. The RMS error in the phase-shift estimate (which can be computed since in simulation we know the true phase shift) versus the upsampling factor of the sinusoidal illumination obtained for different orientations of the sinusoidal illumination is plotted in Fig. 7. The RMS error drops sharply for upsampling factors up to 10 or 15 and then there are smaller improvements after that, on average. This trend in the curve is maintained even in the presence of substantial noise. The curve shown in Fig. 7 used images with Gaussian noise having SNR of 15.5 and for a sinusoid at 50% of cutoff frequency. We tried frequencies up to 93% of cutoff and this trend of improvement in phase-shift estimates for upsampling factors up to 10 to 15 appears for higher frequencies of the sinusoidal illumination as well.

It should be noted here that care needs to be taken while upsampling the Fourier transform of the image. For perfectly vertical or horizontal sinusoidal illumination patterns, the peaks from the sinusoidal illumination in the Fourier domain lie exactly on the f_x or f_y axes. Upsampling methods may exacerbate the ringing effect, from the edges of the image, in the Fourier domain and introduce error in the upsampled phase-shift estimate. So, from this simulation onwards, we used a sinusoidal illumination that is neither exactly vertical nor horizontal: we used sinusoidal illumination that made roughly 11°, 131°, and 251° angles with respect to the vertical f_y axis instead of the 0°, 120°, and 240° orientations we used before. Using a guard band padding the sinusoidally patterned image improves phase-shift estimates for frequencies lying on the f_x or f_y axes. In our simulation results that follow, we use a raised cosine guard band of width 20 pixels surrounding the simulated object.

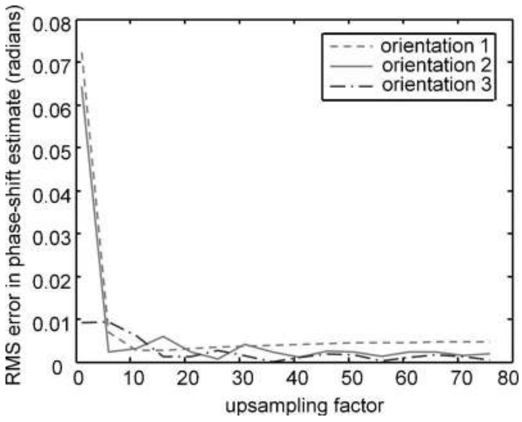

Fig. 7. RMS error in phase-shift estimate versus upsampling factor, $f_o=50\%f_c$, SNR=15.5.

B. Image Reconstruction Examples

These phase-shift estimates can be used to recover the three copies of the object Fourier transform from the N images using singular value decomposition and pseudoinverse [20]. The reconstructed image is formed by appropriate weighting and superposition of the retrieved object spectra as given by Eq. (14). All images discussed in Figs. 8–12 contain no noise. The effect of noise on image reconstruction is discussed at the end of this section.

Figure 8(a) shows a simulated conventional image taken with uniform illumination and Fig. 8(b) shows its Fourier transform. Fig. 9(a) is the OTF-compensated version of the conventional image, given by Eq. (14), and Fig. 9(b) shows its Fourier transform. The detailed features of the bricks and leaves, which were visible in the pristine object shown in Fig. 2(a), cannot be distinguished in ei-

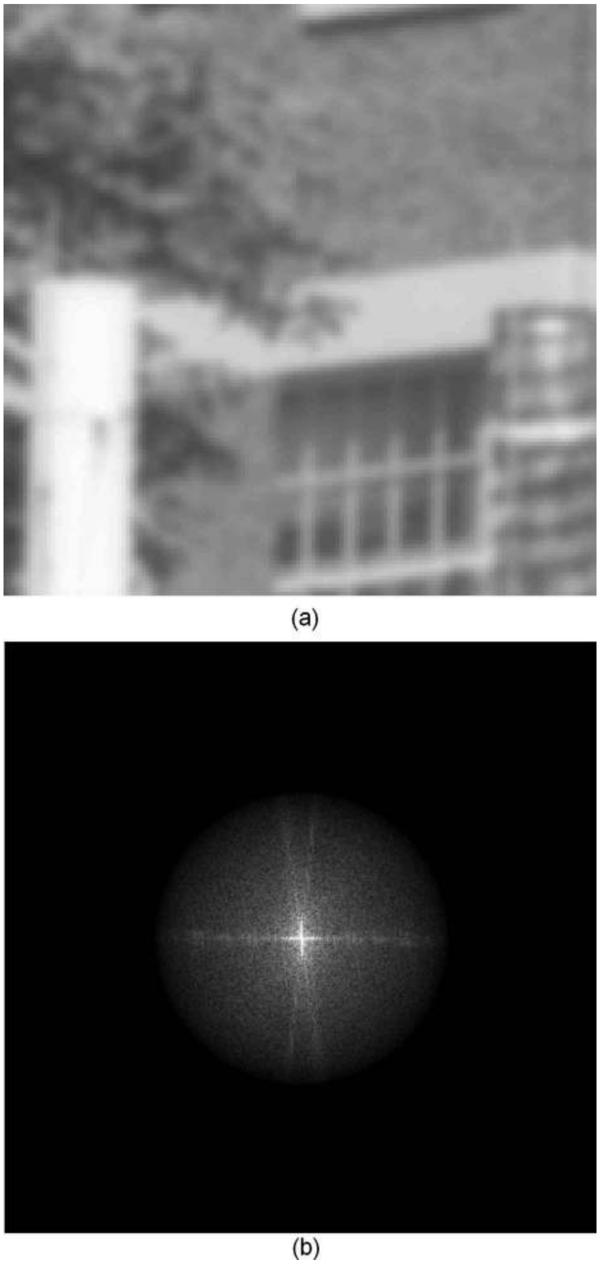

Fig. 8. (a) Conventional image; (b) Fourier transform of conventional image.

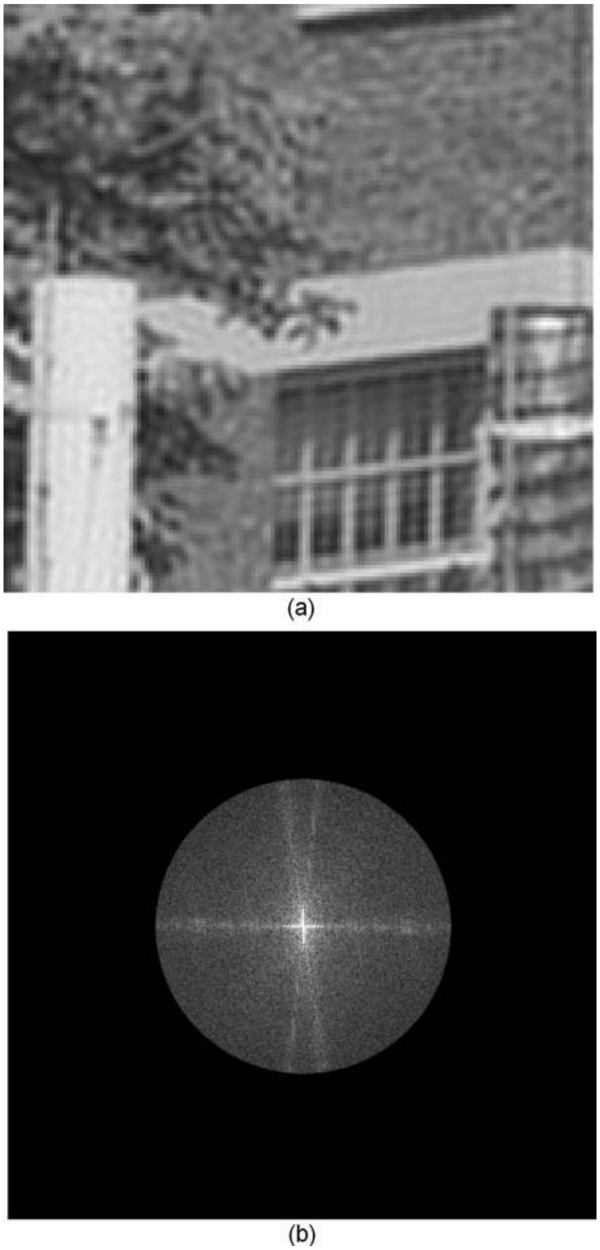

Fig. 9. (a) Conventional image with OTF compensation; (b) Fourier transform of OTF compensated conventional image.

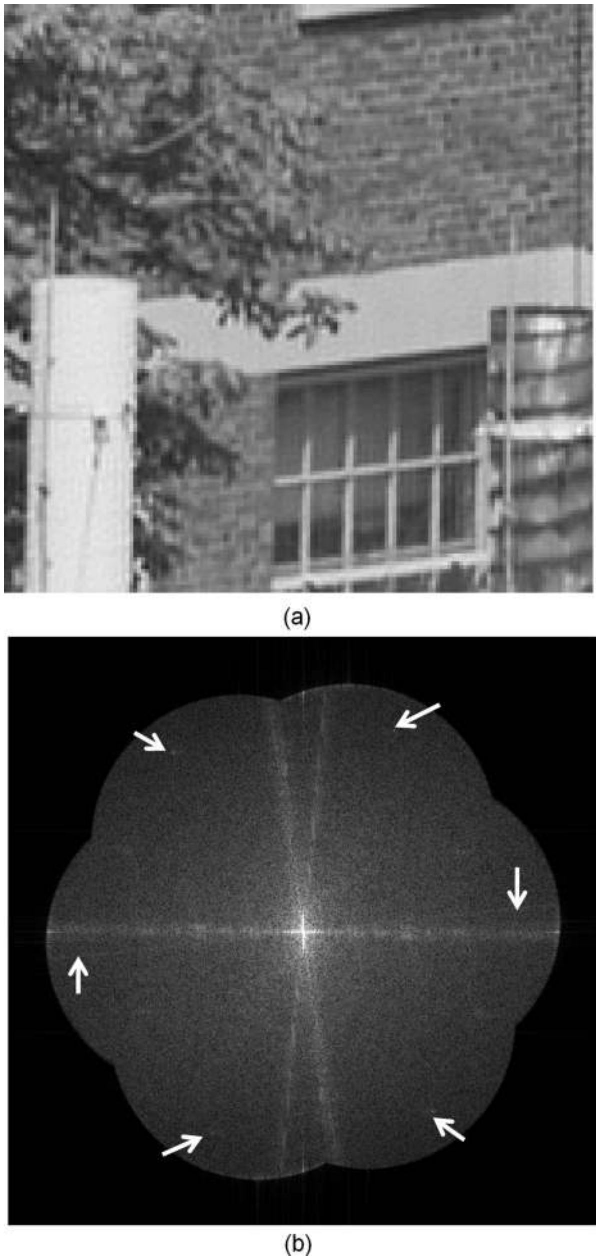

Fig. 10. (a) Image with 75% superresolution, using estimated phase shifts (RMS error less than 4×10^{-3} rad); (b) Fourier transform of image with 75% superresolution, using estimated phase shifts. White arrows indicate locations of potential residual peaks.

ther Figs. 8(a) and 9(a). This is because the spatial frequencies of these fine features of the image lie outside the extent of the conventional OTF, seen in Fig. 8(b), and simple deconvolution does not increase the extent of the OTF of the image as can be seen in Fig. 9(b). Therefore the spatial frequencies containing these fine features of the object are entirely missing in both the conventional image and its OTF-compensated version. Hence, we need superresolution techniques to reveal these fine features of the object.

Figures 10–12 show superresolved reconstructions and their Fourier transforms. We notice a distinct improvement in the resolution of fine details in bricks and leaves in each image. We also observe a corresponding increase in the extent of the effective OTF in the Fourier transforms of the superresolved images. The amount of superresolution (and effective increase in OTF coverage) is directly proportional to the spatial frequency of the sinusoidal illumination in the image. This increase cannot be seen in the Fourier transforms of the conventional image or the deconvolved conventional image shown in Figs. 8(b) and 9(b). Therefore this is indeed optical superresolution we are observing in the images shown in Figs. 10–12. It should be noted that all the Fourier transform figures shown here have been stretched substantially to show dim details such as residual-peak artifacts, which are usually quite dim compared to the maximum in the Fourier transform.

Figure 10(a) shows the OTF-compensated superresolved image having 75% superresolution ($f_o = 75\% f_c$), ob-

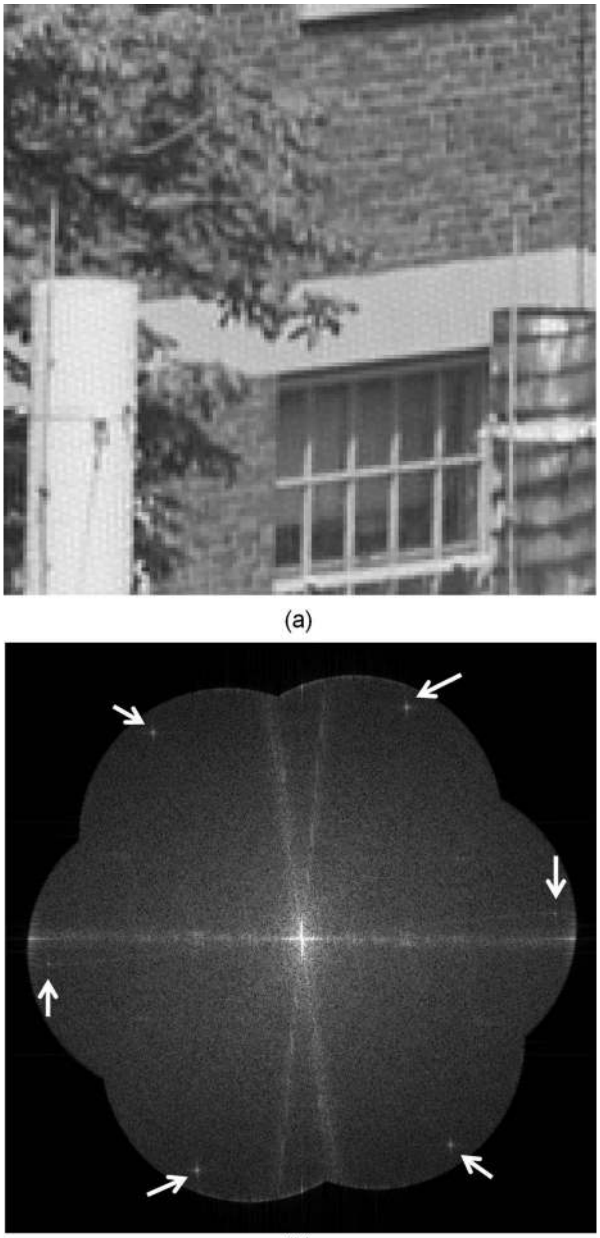
(a)

(b)

Fig. 11. (a) Image with 86% superresolution, estimated phase shifts (RMS error less than 7×10^{-3} rad); (b) Fourier transform of image with 86% superresolution, estimated phase shifts. White arrows indicate locations of dim residual peaks.

tained from three sinusoidally patterned images with randomly spaced phase shifts (−0.4024, 2.0184, 1.0350 rad, i.e., −23.0558°, 115.6458°, 59.3011°.) Here the phase-shift estimation employed 36 times upsampling. There was an RMS error of less than 4×10^{-3} rad for the three orientations of the sinusoidal pattern. We saw no significant artifacts such as residual sinusoidal patterns in the reconstructed image or residual peaks in its Fourier transform shown in Fig. 10(b). If the phase-shift estimate had not been good enough, the Fourier domain would have contained residual-peak artifacts, such as were seen in the case of Fig. 6(b). The locations of possible residual peaks are indicated by white arrows in Fig. 10(b).

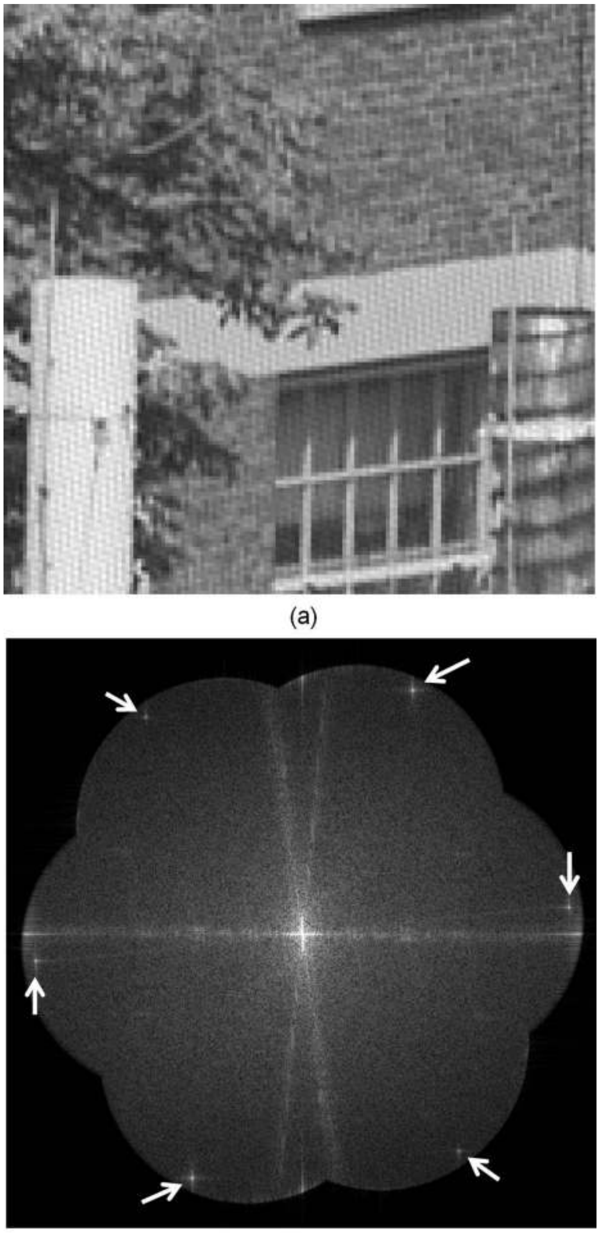
(a)

(b)

Fig. 12. (a) Image with 91% superresolution, estimated phase shifts (RMS error less than 2×10^{-2} rad); (b) Fourier transform of image with 91% superresolution, estimated phase shifts. White arrows indicate locations of residual peaks.

Figure 11(a) shows a reconstruction with 86% superresolution. This was obtained from three sinusoidally patterned images with equally spaced phase shifts (0, 2.0944, 4.1888 rad, i.e., 0°, 120°, and 240°) and the phase-shift estimation employed 36 times upsampling. There was an RMS error of less than 7×10^{-3} rad for each orientation of the sinusoidal illumination. We saw low contrast residual moiré patterned artifacts in the regions having a uniform background in the reconstructed image. Fine features in the image such as the details in the bricks and leaves are important from the perspective of superresolution because they cannot be resolved in the conventional image, but are resolved in this image. The residual artifacts are not apparent on the bricks and leaves in this image. Its

Fourier transform shown in Fig. 11(b) contains dim residual peaks indicated by white arrows.

Figure 12(a) shows a reconstruction with 91% superresolution. This was also obtained from three sinusoidally patterned images with equally spaced phase shifts (0, 2.0944, 4.1888 rad i.e., 0°, 120°, and 240°) and the phase-shift estimation employed 36 times upsampling. There was an RMS error of less than 2×10^{-2} rad for each orientation of the sinusoidal illumination. Here we observe clear residual fringe artifacts throughout the reconstructed image as well as residual peaks, indicated by white arrows, in its Fourier transform shown in Fig. 12(b). Here the residual fringe artifacts are producing a jagged, moiré effect on the edges of the bricks and leaves in this image. There is also a moiré pattern visible in uniform white regions in the image. Usually these fringe artifacts are more clearly perceived as a uniform fringe or checkerboard-type pattern in such uniform backgrounds, reflecting an insufficiently accurate phase-shift estimate.

These results confirm that as long as there is reasonably high contrast in the sinusoidal illumination in the images our phase-shift estimate is accurate enough to provide artifact-free reconstruction. In general we saw in our simulations that for f_o/f_c between 15% and 85% the error in the phase-shift estimate is low and therefore the reconstructed image shows no significant artifacts. But if the contrast of the sinusoidal illumination, and effectively the signal in the reconstructed image, goes down, as was the case for f_o/f_c of 91%, the error in the phase-shift estimate increases and becomes significant enough to result in visible artifacts in the reconstructed image and its Fourier transform.

The effect of noise on phase-shift estimates has been discussed in Subsection 4.A. Now we discuss the effect of noise on the superresolved image reconstructions. Noisy images can be improved by summing multiple image reconstructions to improve the SNR. Figure 13(a) shows a reconstructed image having 75% superresolution. This image has been obtained by processing sinusoidally patterned images having an SNR of 124 (defined as the ratio of the mean of the signal to the standard deviation of noise). Gaussian noise was added in the sinusoidally patterned images. The noise in the measured images results in colored noise in the reconstructed superresolved image. The fine details in the bricks and leaves, which are of importance from the perspective of superresolution, are lost in this noise. The Fourier transform of this reconstruction, shown in Fig. 13(b), shows noise drowning the signal in the periphery of the extended OTF, which contains superresolution information. This part of the image transform contains a signal that has been attenuated proportional to $(m/4)\mathcal{H}_1(2f_o,0)\mathcal{H}_2(2f_o,0)$. Therefore if the contrast of the sinusoidal illumination is low, such as for the case of $f_o=75\%f_c$, then effectively the strength of the superresolution signal is low, and hence the effective SNR is poor. This makes the image reconstruction sensitive to noise at higher spatial frequencies of the sinusoidal illumination.

We can, however, improve the SNR in the superresolved images by summing multiple images, as is commonly done for the case of noisy data. In Fig. 14(a) we have summed 10 image reconstructions with independent noise realizations to obtain a substantially improved image. Here the details in the bricks and leaves are clear and the usefulness of the 75% superresolution is more evident than was in the case of a single noisy reconstruction. The Fourier transform of this image, shown in Fig. 14(b), also shows clearly that now the superresolution signal is stronger in the peripheral regions of the extended OTF. For lower values of superresolution we will need to sum fewer images. The effect of noise is discussed in more detail in [27] where we use the multiframe filter in Eq. (14) to simultaneously add the component images obtained from multiple noise realizations instead of a simple average of multiple image reconstructions shown here.

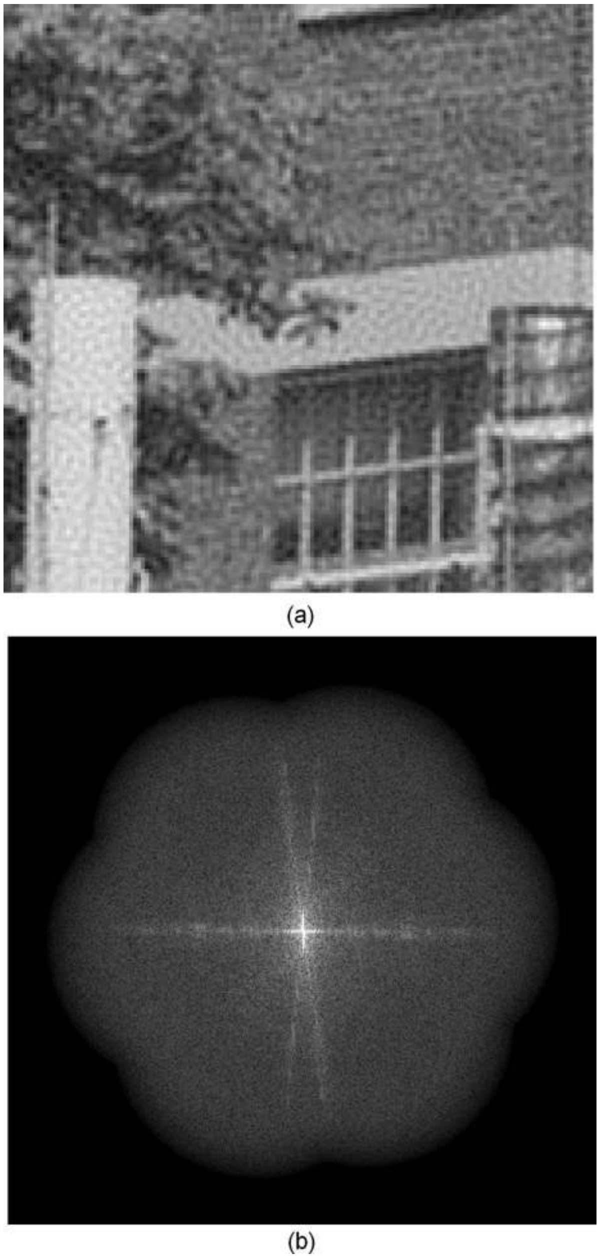

Fig. 13. (a) Single image reconstruction with 75% superresolution from noisy structured illumination images having an SNR of 124, using estimated phase shifts (RMS error less than 0.3 rad); (b) Fourier transform of noisy reconstruction with 75% superresolution.

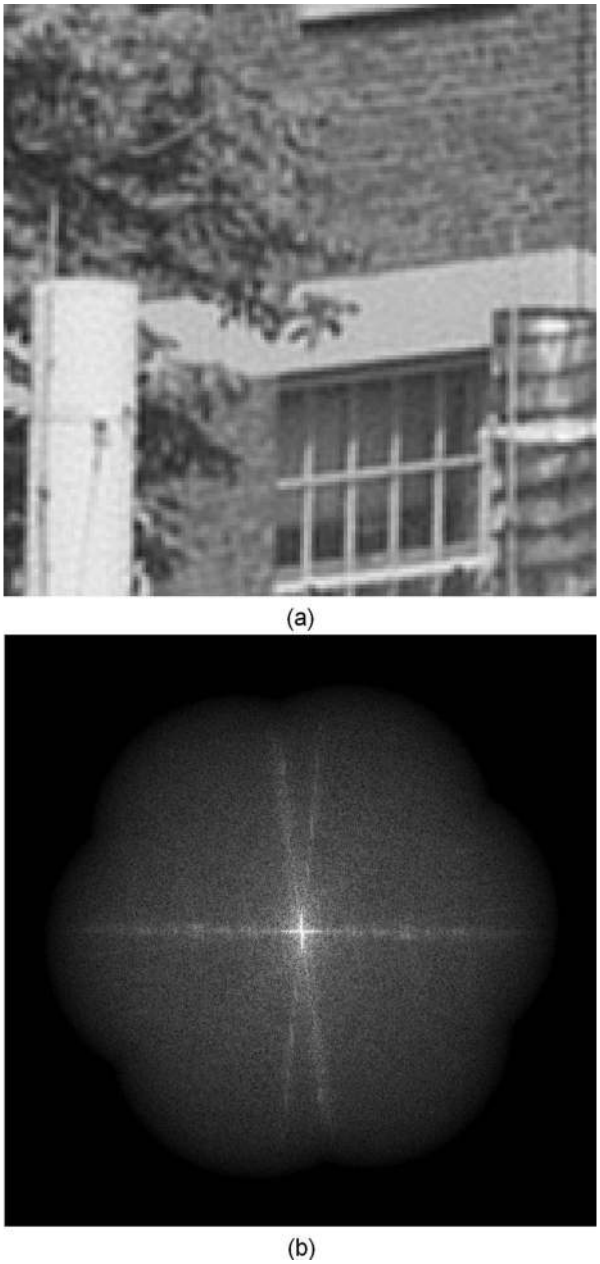

Fig. 14. (a) Sum of 10 noisy images with 75% superresolution, each obtained from sinusoidally patterned images having an SNR of 124, using estimated phase shifts (RMS error less than 0.3 rad); (b) Fourier transform of sum of 10 noisy images with 75% superresolution.

5. CONCLUSIONS

We have developed a method of estimating the phase shift in the sinusoidal illumination pattern for images used to extract superresolution information in fluorescence images. The technique, as demonstrated in this paper, assumes fluorescence or object incoherence. It can be used for both coherent laser fringe illumination as well as incoherent sinusoidal illumination. It can also work for coherent imaging modalities where the object is nonfluorescent, which will be discussed in a future paper. This technique is also directly applicable to the axial sectioning application of sinusoidally illuminated images.

We assume no prior knowledge about the phase shifts in our method. We have shown the phase-shift estimation to be robust to noise. The estimate deteriorates in high noise conditions and for extremely low or extremely high spatial frequencies of the sinusoidal illumination. We have modified the image reconstruction to handle random phase shifts. We have achieved an error less than 10^{-2} rad in our phase-shift estimates for spatial frequencies of the sinusoidal illumination at 15%–85% of cutoff frequency and artifact-free image reconstructions. We have also taken images from a fluorescence microscope and used a sinusoidal illumination to achieve superresolution. These results will be discussed in a future publication. Our estimates can also be used as an initial starting point for optimization routines that minimize residual artifacts in the reconstruction such as shown in [19]. We can estimate unknown spatial frequencies and angular orientations of the sinusoidal illumination. The phase estimation technique is valid for any spatial frequency and angular orientation of the sinusoidal illumination.

Our future work will include imaging moving and nonfluorescent *in vivo* objects, such as a living human retina. The ability to apply such superresolution techniques to moving objects greatly enhances the versatility of structured illumination imaging to encompass a broad range of biological imaging. It opens up areas of dynamic imaging and enables the application of superresolved imaging to *in vivo* clinical imaging, life science research, and biotechnology.

REFERENCES

1. M. Gustaffson, "Surpassing the lateral resolution limit by a factor of two using structured illumination microscopy," J. Microsc. **198**, 82–87 (2000).
2. M. Gustafsson, "Extended-resolution reconstruction of structured illumination microscopy data," in *Adaptive Optics: Analysis and Methods/Computational Optical Sensing and Imaging/Information Photonics/Signal Recovery and Synthesis Topical Meetings* (on CD-ROM), OSA Technical Digest (Optical Society of America, 2005), paper JMA2.
3. M. Gustafsson, L. Shao, D. A. Agard, and J. W. Sedat, "Fluorescence microscopy without resolution limit," in *Biophotonics/Optical Interconnects and VLSI Photonics/WBM Microcavities, 2004 Digest of the LEOS Summer Topical Meetings* (IEEE, 2004), Vol. 2, pp. 28–30.
4. R. Heintzmann and C. Cremer, "Laterally modulated excitation microscopy: Improvement of resolution by using a diffraction grating," Proc. SPIE **3568**, 185–196 (1999).
5. M. Gustafsson, "Extended resolution fluorescence microscopy," Curr. Opin. Struct. Biol. **9**, 627–634 (1999).
6. W. Lukosz, "Optical systems with resolving powers exceeding the classical limits II," J. Opt. Soc. Am. **57**, 932–941 (1967).
7. D. Mendlovic, A. W. Lohmann, N. Konforti, I. Kiryuschev, and Z. Zalevsky, "One-dimensional superresolution optical system for temporally restricted objects," Appl. Opt. **36**, 2353–2359 (1997).
8. E. Sabo, Z. Zalevsky, D. Mendlovic, N. Konforti, and I. Kiryuschev, "Superresolution optical system using three fixed generalized gratings: experimental results," J. Opt. Soc. Am. A **18**, 514–520 (2001).
9. A. Shemer, Z. Zalevsky, D. Mendlovic, N. Konforti, and E. Marom, "Time multiplexing superresolution based on interference grating projection," Appl. Opt. **41**, 7397–7404 (2002).
10. S. W. Hell and J. Wichmann, "Breaking the diffraction

resolution limit by stimulated emission: stimulated-emission-depletion fluorescence microscopy," Opt. Lett. **19**, 780 (1994).

11. X. Chen and S. R. J. Brueck, "Imaging interferometric lithography: approaching the resolution limits of optics," Opt. Lett. **24**, 124–126 (1999).
12. C. J. Schwarz, Y. Kuznetsova, and S. R. J. Brueck, "Imaging interferometric microscopy," Opt. Lett. **28**, 1424–1426 (2003).
13. V. Mico, Z. Zalevsky, and J. García, "Superresolution optical system by common-path interferometry," Opt. Express **14**, 5168–5177 (2006).
14. G. E. Cragg and P. T. C. So, "Lateral resolution enhancement with standing evanescent waves," Opt. Lett. **25**, 46–48 (2000).
15. E. Chung, D. Kim, and P. T. So, "Extended resolution wide-field optical imaging: objective-launched standing-wave total internal reflection fluorescence microscopy," Opt. Lett. **31**, 945–947 (2006).
16. T. Wilson and C. J. R. Sheppard, *Theory and Practice of Scanning Optical Microscopy* (Academic, 1983).
17. M. A. A. Neil, R. Juskaitis, and T. Wilson, "Method of obtaining optical sectioning by using structured light in a conventional microscope," Opt. Lett. **22**, 1905–1907 (1997).
18. M. A. A. Neil, R. Juškaitis, and T. Wilson, "Real time 3D fluorescence microscopy by two beam interference illumination," Opt. Commun. **153**, 1–4 (1998).
19. L. H. Schaefer, D. Schuster, and J. Schaffer, "Structured illumination microscopy: artefact analysis and reduction utilizing a parameter optimization approach," J. Microsc. **216**, 165–174 (2004).
20. G. Strang, *Linear Algebra and Its Applications* (Thomson Learning, Inc., 1998).
21. L. P. Yaroslavsky and H. J. Caulfield, "Deconvolution of multiple images of the same object," Appl. Opt. **33**, 2157–2162 (1994).
22. D. J. Tolhurst, Y. Tadmore, and T. Chao, "Amplitude spectra of natural images," Ophthalmic Physiol. Opt. **12**, 229–232 (1992).
23. A. van der Schaaf and J. H. van Hateren, "Modelling the power spectra of natural images: statistics and information," Vision Res. **36**, 2759–2770 (1996).
24. D. R. Gerwe, M. Jain, B. Calef, and C. Luna, "Regularization for nonlinear image restoration using a prior on the object power spectrum," Proc. SPIE **5896**, 1–15 (2005).
25. J. R. Fienup, D. Griffith, L. Harrington, A. M. Kowalczyk, J. J. Miller, and J. A. Mooney, "Comparison of reconstruction algorithms for images from sparse-aperture systems," Proc. SPIE **4792**, 1–8 (2002).
26. C. W. Helstrom, "Image restoration by the method of least squares," J. Opt. Soc. Am. **57**, 297–303 (1967).
27. S. A. Shroff, J. R. Fienup, and D. R. Williams, "OTF compensation in structured illumination superresolution images," Proc. SPIE **7094**, 709402 (2008).
28. S. A. Shroff, J. R. Fienup, and D. R. Williams, "Phase shift estimation in structured illumination imaging for lateral resolution enhancement," in *Adaptive Optics: Analysis and Methods/Computational Optical Sensing and Imaging/Information Photonics/Signal Recovery and Synthesis Topical Meetings* (on CD-ROM), OSA Technical Digest (Optical Society of America, 2007), paper SMA2.
29. S. A. Shroff, J. R. Fienup, and D. R. Williams, "Estimation of phase shifts in structured illumination for high resolution imaging," in *Frontiers in Optics*, OSA Technical Digest (CD) (Optical Society of America, 2007), paper FMH4.
30. P. Artal, S. Marcos, R. Navarro, and D. R. Williams, "Odd aberrations and double-pass measurements of retinal image quality," J. Opt. Soc. Am. A **12**, 195–201 (1995).
31. M. Guizar-Sicairos, S. T. Thurman, and J. R. Fienup, "Efficient image registration algorithms for computation of invariant error metrics," in *Adaptive Optics: Analysis and Methods/Computational Optical Sensing and Imaging/Information Photonics/Signal Recovery and Synthesis Topical Meetings* (on CD-ROM), OSA Technical Digest (Optical Society of America, 2007), paper SMC3.
32. M. Guizar-Sicairos, S. T. Thurman, and J. R. Fienup, "Efficient subpixel image registration algorithms," Opt. Lett. **33**, 156–158 (2008).